

High energy and power density TiO₂ nanotube electrodes for 3D Li-ion microbatteries†Cite this: *J. Mater. Chem. A*, 2013, **1**, 8160Wei Wei,^{*a} Gabriel Oltean,^a Cheuk-Wai Tai,^b Kristina Edström,^a Fredrik Björefors^a and Leif Nyholm^a

Highly ordered anodic TiO₂ nanotube arrays with a tube length of 9 μm are shown to provide areal capacities of 0.24 mA h cm⁻² (*i.e.* 96 mA h g⁻¹) at a charge/discharge current density of 2.5 mA cm⁻² (corresponding to a rate of 5 C) and 0.46 mA h cm⁻² (*i.e.* 184 mA h g⁻¹) at 0.05 mA cm⁻², when used as 3D free-standing anodes in Li-ion microbatteries. The present nanotube electrodes, which could be cycled for 500 cycles with only 6% loss of capacity, exhibited significantly higher energy and power densities, as well as an excellent cycling stability compared to previously reported TiO₂-based Li-ion microbattery electrodes. The influence of parameters such as ordering, geometry and crystallinity of the nanotubes on the microbattery performance was investigated. A two-step anodization process followed by annealing of the nanotubes was found to yield the best microbattery performance. It is also demonstrated that the rate capability of the electrode depends mainly on the rate of the structural rearrangements associated with the lithiation/delithiation reaction and that the areal capacity at various charge/discharge rates can be increased by increasing the tube wall thickness or the length of the nanotubes, up to 0.6 mA h cm⁻² for 100 cycles.

Received 29th March 2013

Accepted 8th May 2013

DOI: 10.1039/c3ta11273j

www.rsc.org/MaterialsA

1 Introduction

Over the past decades, primary and rechargeable thin-film Li-ion microbatteries with thicknesses up to 100 μm have become the dominant power sources for a wide variety of miniature electronic devices and implantable medical devices.^{1–3} Nevertheless, due to the increasing power requirements of the latter devices and emerging technologies (*e.g.*, wireless transmission), there is a growing need for new microbatteries providing higher energy and power densities. These requirements are, however, more and more difficult to meet using present 2D thin-film Li-ion microbatteries, made by stacking compact thin-film electrodes, electrolytes/separators and current collectors.^{3,4} Although the energy density (or areal capacity per footprint area, mA h cm⁻²) of the thin-film electrode can be increased by increasing the electrode thickness, this decreases the power density (*i.e.*, the capacity at high charge/discharge rates) as a result of the increased transport lengths for the Li⁺ ions. To maximize the energy and power densities of a microbattery with a small (*e.g.*, <1 cm²) footprint area, while maintaining short Li⁺ ion transport distances, the 3D Li-ion microbattery concept has

been proposed.^{3,4} In the latter devices, the battery components – current collectors, electrodes, and electrolytes – are incorporated into a 3D micro- or nanoarchitecture.

Due to the limited packing size of microbatteries as well as high safety requirements, both 2D and 3D microbattery electrodes are normally free-standing structures lacking binders and conductive additives.^{1,5} The electrodes are therefore rather different compared to the composite powder/binder electrodes employed in conventional Li-ion batteries, which complicate the electrode fabrication process. To date, various approaches^{5–7} have been dedicated to the fabrication of free-standing 3D micro- and nano-architected thin-film electrodes, including the use of template-based spray-coatings,⁸ atomic layer deposition (ALD),^{9,10} electrodeposition,¹¹ electrophoretic deposition,¹² and lithographic methods.¹³ The research has so far mainly been focused on the development of 3D electrodes rather than full 3D-microbatteries since the attainment of 3D electrodes with both high areal capacities and high rate capabilities, in addition to long term cycling stability, is still not straightforward.

Among the 3D electrode fabrication methods, self-organized electrochemical anodization has been shown to constitute a straightforward and facile approach as it allows free-standing transition metal oxide nanoarchitectures with high aspect ratios to be formed directly on metal substrates.¹⁴ By anodization of metal sheets in dilute fluoride-containing organic electrolytes, vertically aligned, well-defined TiO₂,¹⁴ Nb₂O₅,¹⁵ and Fe₂O₃ nanotube arrays¹⁶ with tuneable sizes have been formed.

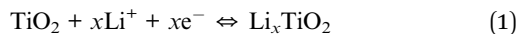
^aDepartment of Chemistry – Ångström Laboratory, Uppsala University, Box 538, SE-75121, Uppsala, Sweden. E-mail: wei.wei@kemi.uu.se; Fax: +46 018 513548; Tel: +46 018 4713700

^bDepartment of Materials and Environmental Chemistry, Arrhenius Laboratory, Stockholm University, SE-10691, Stockholm, Sweden

† Electronic supplementary information (ESI) available: Additional experimental data. See DOI: 10.1039/c3ta11273j

Other direct growth approaches without template assistance, such as the alkali hydrothermal process,¹⁷ on the other hand, are time-consuming and it is difficult to tailor the size of the obtained oxide nanostructures.

Bulk or nanostructured TiO₂ (nanoparticles, nanotubes, nanowires, *etc.*) have been widely investigated as electrode materials for conventional Li-ion batteries (*i.e.* in the form of composite electrode containing TiO₂ powders, binders and additives),^{18–25} based on the following redox reaction:



In the reduction of Ti⁴⁺ to Ti³⁺, accompanied by Li⁺ insertion, anatase TiO₂ can reversibly accommodate Li⁺ to yield Li_{0.5}TiO₂, which provides a specific capacity of 168 mA h g^{−1}.^{22,23} Only recently, some free-standing TiO₂ nanotube arrays, either pristine TiO₂ nanotubes^{26–30} or composite TiO₂ nanotube electrodes filled with other oxide or polymer nanostructures,^{31–34} have been employed to construct 3D Li-ion microbatteries. Despite the uncomplicated and template-free fabrication process, the attained areal capacities of the electrodes, particularly at high charge/discharge rates, were, however, still rather low (*e.g.*, <0.15 mA h cm^{−2} at the highest charge/discharge current density of 1 mA cm^{−2}) and long-term cycling stability results were not reported. It is therefore clear that more in-depth work is needed to be able to exploit free-standing TiO₂ nanotube arrays as high energy and power density electrodes for 3D Li-ion microbatteries.

In the present work, we demonstrate that by using highly ordered anatase TiO₂ nanotube array electrodes with a high (*i.e.* 60) aspect ratio, areal capacities of 0.24 mA h cm^{−2} (*i.e.* gravimetric capacities of 96 mA h g^{−1}) at a charge/discharge current density of 2.5 mA cm^{−2}, and 0.46 mA h cm^{−2} (*i.e.* 184 mA h g^{−1}) at 0.05 mA cm^{−2} can be achieved. It is also shown that 94% of the initial capacity was retained after 500 cycles, indicating that the present TiO₂ nanotube electrodes, which were formed by a simple two-step anodization approach followed by annealing, exhibit superior performance when compared to previously reported pristine or composite TiO₂-based microbattery electrodes as well as other types of microbattery electrodes. The influence of the length and wall thickness of the nanotubes on the areal capacity and stability is also discussed, as well as the factors limiting the rate capability of Li-ion microbatteries based on this kind of nanotube electrodes.

2 Experimental section

Formation of anodic TiO₂ nanotubes

Prior to anodization, the titanium foils (0.1 mm thick, 99.9% purity, Goodfellow) were cut into 10 mm × 10 mm pieces and cleaned by sonication in ethanol for 5 min, followed by rinsing with deionized (DI) water and drying in a flow of nitrogen. The electrolytes were prepared from ethylene glycol (99.5% purity, <0.1 wt% of H₂O) mixed with DI water (5 vol%) and also contained NH₄F (0.1 M or 0.3 M). All electrolytes were prepared from reagent grade chemicals (Sigma-Aldrich).

All anodic oxidation processes were carried out at room temperature using a two-electrode system. A platinum flag placed 1 cm from the (Ti foil) working electrode, served as the counter electrode. The anodization experiments were carried out with a DC power source (ES075-2, Delta Elektronika), by stepping the potential from zero to the final potential after which the final potential was maintained for 20–120 min. In the one-step anodization formation process, the anodization was carried out at 60 V for 1.5 hours to obtain 9 μm long nanotubes. For the two-step anodization process, the first anodization was carried out for 4 hours, after which the obtained nanotube layer was removed by strong sonication in DI water for 20 min to expose the underlying textured Ti substrate. The second anodization was performed on this textured Ti substrate for 20 min (4.5 μm long nanotubes), 1 hour (9 μm long ones) or 2 hours (14.5 μm long ones) under the same conditions. After the anodization, the samples were rinsed in DI water and finally dried in a flow of nitrogen.

For the thin wall nanotubes formed by post-chemical etching, these nanotube samples after the anodic formation were placed in a stirred NH₄F (0.2 M) aqueous solution at 30 °C for 4 hours. Another type of thin wall nanotube was formed by two-step anodization of Ti under modified conditions, that is, in an ethylene glycol electrolyte containing DI water (5 vol%) and NH₄F (0.3 M) at 50 V for 2.5 hours. After the anodization, the samples were rinsed in DI water and sonicated for 10 min to remove the top nanograss layer, prior to drying in a flow of nitrogen.

To crystallize the as-formed TiO₂ layers, some samples were thermally annealed at 350 °C in air for 5 hours. In all the cases, the heating from room temperature to 350 °C was carried out at a rate of 6 °C min^{−1}. The samples were left to cool down within the oven.

Materials characterization

A high resolution scanning electron microscope (SEM, Zeiss 1550) was used to characterize the structure of the obtained anodic TiO₂ films. Cross-sectional measurements were carried out on mechanically cracked samples. X-ray diffractometry (XRD) was employed for crystalline characterization of the as-formed/annealed nanotube layers using a grazing angle of 1°, with a Siemens 5000D diffractometer employing monochromatic Cu Kα radiation. The transmission electron microscope (TEM) characterization was carried out at room temperature with a JEOL JEM-2100F microscope operated at 200 kV. The grown nanotubes were scratched from the substrate employing a diamond scribe and the flakes were placed on a Cu grid using a porous carbon supporting film. The thermal gravimetric analysis (TGA) of as-formed nanotubes was performed using a TGA Q500 analyzer with an air flow rate of 20 ml min^{−1} and a heating rate of 6 °C min^{−1} from room temperature to 375 °C. Prior to the TGA experiments, ~20 mg as-formed TiO₂ nanotubes were dried in a vacuum at 120 °C for 12 hours to remove the physically absorbed moisture. The nanotubes were then scratched off from the substrate.

Battery assembly and testing

All the TiO_2 nanotube electrodes were electrochemically tested against metallic lithium foils in polymer coated aluminium pouch cells. The cells were assembled in an argon filled glove box (MBraun, H_2O , $\text{O}_2 < 2$ ppm). TiO_2 nanotube electrodes served as the working electrodes while lithium foils served as the counter and reference electrodes. The two electrodes were separated by a glass fibre separator (Whatman) soaked with 1 M LiClO_4 in propylene carbonate solution (Sigma-Aldrich). Prior to the cell assembly, the TiO_2 nanotube electrodes were dried in a vacuum oven in the glove box at 120°C for 12 hours. Unless otherwise specified, the cells were galvanostatically cycled between 1.5 and 2.5 V vs. Li^+/Li using an Arbin battery tester at a C/10 rate, *i.e.* full charge/discharge in 10 hours.

Cyclic voltammograms for the TiO_2 nanotube/Li cells were recorded using a VMP2 potentiostat/galvanostat. The potential was first scanned from open circuit voltage (OCV) to 1.2 V (or 1.5 V at low rates) vs. Li^+/Li , then to 2.7 V (or 2.5 V at low rates) vs. Li^+/Li and finally back to the OCV. The scan rate was varied between 0.001 and 5 mV s^{-1} .

3 Results and discussion

An example of the high aspect ratio, highly ordered TiO_2 nanotube arrays obtained by the anodization approach is shown in the SEM micrograph in Fig. 1 and the TEM

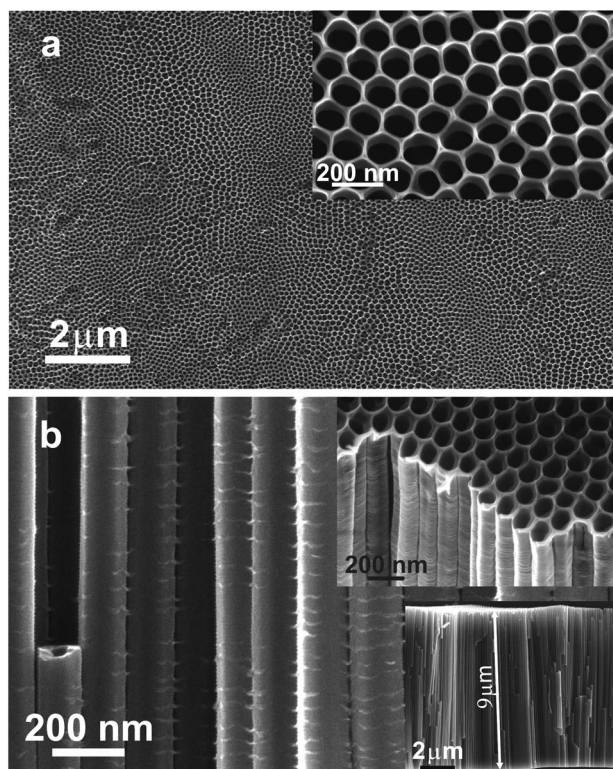


Fig. 1 SEM micrographs depicting a self-ordered TiO_2 nanotube layer formed by two-step anodization of a Ti foil, where (a) depicts a large area top-view and (b) a cross-sectional view. The inset in (a) shows a high magnification top-view whereas the insets in (b) show a high magnification cross-sectional view at the tube top as well as the tube length.

micrograph in Fig. 2. The $9\text{ }\mu\text{m}$ thick nanotubular TiO_2 layer was grown on a titanium foil by anodization in a 0.2 M NH_4F and 5 vol% H_2O containing ethylene glycol electrolyte at 60 V for 1 hour. From the top and cross-sectional views in Fig. 1, it is evident that the formed nanotubes, exhibiting an average inner diameter and tube wall of $\sim 50\text{ nm}$, were well-aligned, oriented perpendicular to the substrate and uniformly distributed over the entire anodized area. The diameter of the nanotubes can be altered by adjusting the anodization conditions, *e.g.*, the voltage and/or fluoride concentration of the electrolyte, while the nanotube length can be increased by prolonging the anodization time. In the present case, TiO_2 nanotubes with a maximum length of $\sim 20\text{ }\mu\text{m}$ could be obtained after a sufficiently long anodization time.

A two-step anodization process was employed in the formation of nanotubes since this has been shown to improve the long-range ordering of the nanotube array system.³⁵ Nanotubes manufactured using a one-step anodization procedure were, however, also studied for comparison. More details regarding the anodic oxidation processes are given in the ESI, Fig. S1.† As

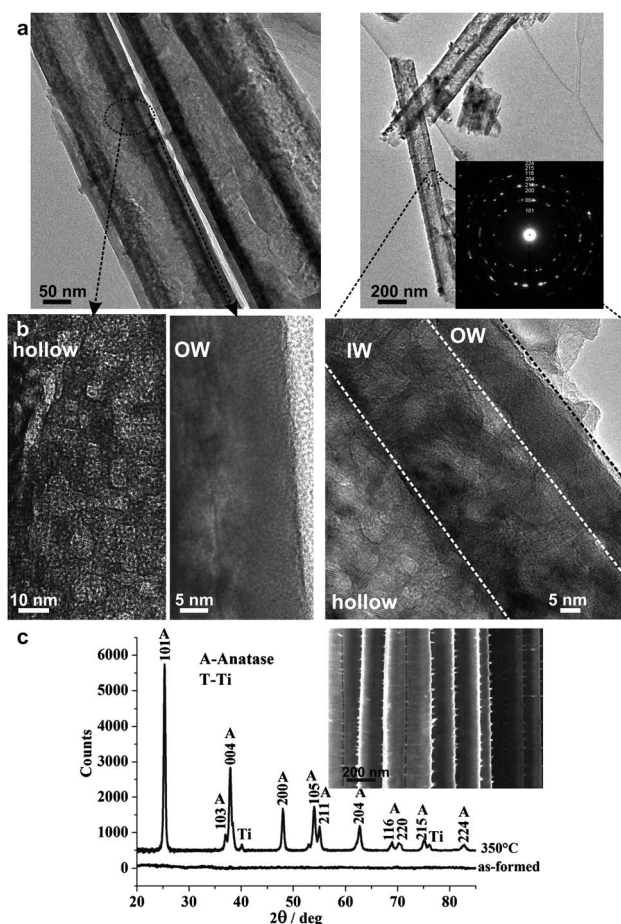


Fig. 2 (a) BF-TEM and (b) HRTEM micrographs of annealed nanotube bundles (left) and a single nanotube (right). The HRTEM micrographs were taken at the hollow, OW and IW parts of a single tube. The inset of (a) (right micrograph) shows the SAED pattern of the annealed nanotubes. (c) XRD patterns of the annealed and as-formed TiO_2 nanotube electrodes, respectively. The inset shows the cross-sectional SEM image of annealed nanotubes.

shown in Fig. 1b, a hexagonal nano-ring network, which linked the individual nanotubes into a continuous thin film, remained at the top of the nanotubes after the two-step anodization process.

The SEM micrographs of the one-step anodized TiO₂ nanotube film, depicted in Fig. S2a and b in the ESI,[†] on the other hand, clearly show that these films only exhibited short-range ordering, several cracks as well as remaining irregular pore/tube layers (on the tube tops). It is therefore evident that the two-step anodization approach provides not only more long-range ordered nanotube systems than the one-step procedure,³⁵ but also better contact between the individual tubes.

As shown by the XRD diffractograms in Fig. 2c, the as-formed, two-step anodized TiO₂ nanotubes were amorphous since no peaks could be seen. However, by annealing the sample at 350 °C in air for 5 hours, polycrystalline TiO₂ nanotubes were obtained. It is seen in the diffractogram that the thermal treatment mainly resulted in the formation of anatase (JPCDS 21-1272). TGA of the as-formed, two-step anodized TiO₂ nanotubes demonstrated a ~1.5% sample weight loss between 180 °C and 280 °C (see the ESI, Fig. S3a[†]), mostly due to dehydration of the TiO₂ nanotubes.³⁶

The annealed, two-step anodized TiO₂ nanotube arrays were further characterized using TEM. Fig. 2a shows bright-field (BF)-TEM micrographs of nanotube bundles (left) and a single nanotube (right), respectively, as well as the SAED pattern on a single tube. Clearly, the tube walls of the annealed nanotubes contained two types of crystalline layers: the inner wall (IW)

layer and the outer wall (OW) layer, in agreement with previous reports.³⁷ The ~15 nm thick OW layer was composed of crystallites with lengths of several tens of nanometers oriented in the direction of the nanotube axis, as shown in the high-resolution TEM (HRTEM) micrographs in Fig. 2b. The IW layer had a thickness of ~32 nm and contained TiO₂ crystallites with an average size of ~10 nm. The HRTEM micrographs in Fig. 2b and SEM micrograph in Fig. 2c further demonstrate that no cracks could be observed in the OW layers of the nanotubes after annealing at 350 °C. Cracks have, however, been found to form in the OW layers if the annealing temperature is too high (*e.g.*, more than 450 °C).^{14,37} In Fig. 2 it is also seen that the tube wall thickness was still ~50 nm after the annealing treatment.

The battery performances of the as-formed and annealed, one- and two-step anodized TiO₂ nanotube arrays were tested in cells containing the nanotube electrodes as working electrodes and lithium foil as the counter electrodes, as well as a glass fibre separator soaked with a 1 M LiClO₄/propylene carbonate electrolyte. Fig. 3a exhibits the galvanostatic areal capacities as a function of the cycle number for four different TiO₂ nanotube containing cells, recorded in the potential range 1.5–2.5 V at a cycling rate of C/10 (*i.e.* full charge/discharge in 10 h). It is seen that the cell containing the annealed, two-step anodized TiO₂ nanotube electrode provided the highest and most stable areal capacity of 0.46 mA h cm⁻² over 100 cycles, using a constant current density of 0.05 mA cm⁻². The cell comprising the annealed, one-step anodized TiO₂ nanotube electrode, on the other hand, showed an initial areal capacity of ~0.40 mA h cm⁻²

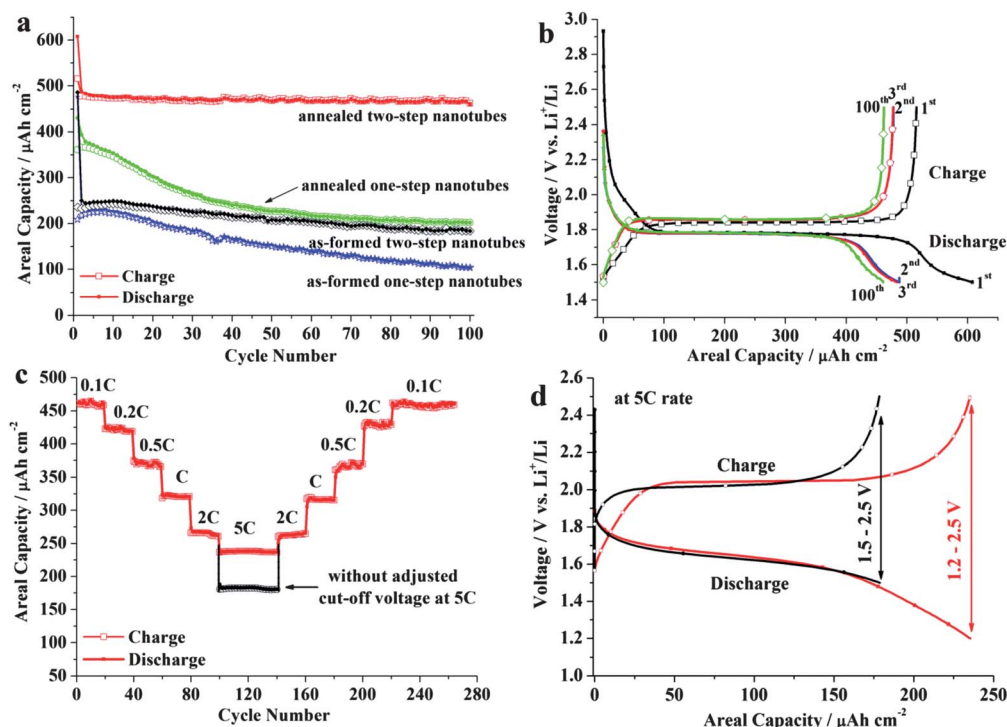


Fig. 3 (a) Galvanostatic areal charge (open symbol, *e.g.*, \square) and discharge (solid symbol, *e.g.*, \blacksquare) capacities as a function of the cycle number for different TiO₂ nanotube electrodes obtained at a C/10 cycling rate. (b) Charge and discharge curves for the 1st, 2nd, 3rd and 100th cycles for the annealed, two-step anodized TiO₂ nanotube electrode. (c) Rate capability for the annealed, two-step anodized TiO₂ nanotube electrode. (d) Charge and discharge curves for the annealed, two-step anodized TiO₂ nanotube electrode at a 5 C rate for cycling between 1.2 and 2.5 V, and between 1.5 and 2.5 V vs. Li⁺/Li, respectively.

but gradually lost capacity during the cycling. In this case the loss was $\sim 50\%$ over 100 cycles.

The poor cycling stability of the annealed, one-step anodized nanotube electrode cell compared to its two-step anodized analogue may be due to a gradual loss of contact with the nanotubes as a result of the remaining stress, as well as the weak link between the neighbouring nanotubes. It is well-known that the Li^+ ion insertion and extraction give rise to volume expansion and contraction of the host material, although the volume expansion effect is relatively small (*i.e.* 3–4%) for $\text{TiO}_2/\text{Li}_{0.5}\text{TiO}_2$.³⁸ Another possibility is that the migration of Li^+ ions within the irregular nanotube system is less facile than for the highly ordered, two-step anodized nanotubes. As shown in Fig. S2e in the ESI,[†] for the annealed, one-step anodized TiO_2 nanotube layer, parts of the nanotube layer were found to have detached from the Ti substrate after the cycling experiments. For the remaining nanotube layers, many new and big cracks could also be observed in the SEM micrographs (see Fig. S2a and b in the ESI[†]).

These findings indicate that the capacity loss for the one-step anodized nanotubes was due to a loss of contact with the nanotubes as a result of the stress invoked by the repeated Li^+ ion insertion and extraction. For the highly ordered, two-step anodized nanotube layer, the long-range ordering of the nanotube array probably suppresses the effects of such stress while the continuous nano-ring layer on the top of the nanotubes significantly enhances the connection between the individual nanotubes. This explains why the areal capacity could be maintained during the long-term cycling for the two-step anodized nanotube electrodes.

Compared to the cells comprising annealed nanotubes, both the as-formed, one- and two-step anodized TiO_2 nanotube containing cells exhibited significantly lower initial capacities, *i.e.* $\sim 0.20 \text{ mA h cm}^{-2}$ as shown in Fig. 3a. The capacities of the as-prepared nanotube electrodes were also found to decrease upon cycling, with the largest decrease being observed for the one-step anodized nanotube electrode.

These results indicate that the cycling stability for the TiO_2 nanotube electrodes depends on both the anodization procedure and annealing treatment, as these procedures affect the long-range ordering of the tube system and the contact between the tubes as well as the crystallinity. The results thus clearly show that the annealed nanotube electrodes provided higher capacities than the corresponding amorphous as-prepared ones. This finding is in contrast to other reports,^{27–29} where amorphous TiO_2 nanotube electrodes yielded slightly higher areal capacities than annealed ones. This could be explained by the fact that thinner wall ($< 20 \text{ nm}$) nanotubes and different annealing temperatures (*e.g.*, 450°C) were used in these studies. It should also be pointed out that the areal capacities of both the as-prepared and annealed electrodes were significantly lower, *i.e.* $< 0.17 \text{ mA h cm}^{-2}$, in these reports than in the present case.

Charge and discharge curves for the annealed, two-step anodized TiO_2 nanotube electrode at a rate of $C/10$ are shown in Fig. 3b. On the first discharge (*i.e.* lithiation) and charge (*i.e.* delithiation) well-defined plateaus at about 1.78 and 1.84 V vs.

Li^+/Li , respectively, can be observed due to the insertion of Li^+ into the tetragonal anatase phase and extraction of Li^+ from the Li-rich orthorhombic Li_xTiO_2 phase, respectively.^{18,38} It is seen that the first discharge and charge capacities were 0.61 and $0.52 \text{ mA h cm}^{-2}$, respectively, whereas the discharge capacity stabilized at $\sim 0.48 \text{ mA h cm}^{-2}$ after the second cycle yielding a coulombic efficiency (*i.e.* charge capacity/discharge capacity) of 98% on the second cycle.

As shown in Fig. S3b in the ESI,[†] the shapes of the corresponding charge and discharge curves for the as-prepared, two-step anodized nanotube electrode were very different from those for annealed nanotube electrodes, as no well-defined plateaus could be seen. A larger irreversible first cycle capacity loss, *i.e.* $\sim 51\%$, was also seen in this case (whereas the corresponding value for the annealed ones was about 15%) as well as a larger decrease in the capacity as a function of the cycle number. Since the irreversible capacity loss on the first cycle is unlikely to be due to the solid-electrolyte interphase (SEI) formation (as the SEI formation generally takes place at significantly lower potential³⁹), this initial capacity loss could be ascribed either to trapping of Li^+ inside the nanotubes, the presence of small amounts of residual water in the tubes (as shown by the previous TGA results) or an initial loss of contact with some remaining disordered parts of the nanotube systems. The results for the as-formed tubes also suggest that the lithiation and delithiation of these as-prepared nanotubes is associated with an overpotential which increases gradually during the charging (reduction reaction) and discharging (oxidation reaction) steps. This could originate from the lack of crystallinity of the nanotubes yielding a chronopotentiogram similar to that for a material with supercapacitive behaviour.²³

To reach a better understanding of the electrochemical behaviour of the present nanotube electrode it is important to evaluate how much of the TiO_2 present in the nanotubes is actually employed during the lithiation and delithiation reactions. Assuming that the nanotubes are perfectly hexagonally arranged over the entire substrate area, with a length of $9 \mu\text{m}$, a tube inner diameter of 50 nm and a tube wall thickness of 50 nm , $6.28 \times 10^{-4} \text{ cm}^3$ of TiO_2 with a surface area of 252.6 cm^2 is obtained for a footprint area of 1 cm^2 . As this corresponds to $2.51 \times 10^{-3} \text{ g}$ of anatase (assuming a density of 4.0 g cm^{-3}), an areal capacity of about $0.42 \text{ mA h cm}^{-2}$ is expected based on a theoretical capacity of 168 mA h g^{-1} . Given the experimentally obtained areal capacity of $0.460 \text{ mA h cm}^{-2}$ (see Fig. 3a, *i.e.* gravimetric capacity of 184 mA h g^{-1}), it is hence reasonable to assume that all the available TiO_2 in the annealed, two-step anodized nanotubes was electrochemically active during the charge/discharge steps. It can also be concluded that the double layer charging contribution²³ to the areal capacity should be smaller than 0.5%, despite the fact that the surface area enhancement factor was as large as about 250.

The rate capability and cycle stability of the annealed, two-step anodized TiO_2 nanotube electrode were further evaluated. As shown in Fig. 3c, it is clear that the areal capacities of the present nanotube electrode were very stable during 40 cycles at various cycling rates and that the capacities were found to be the same for a specific rate even after the rate capability

experiments. This indicates that no degradation of the nanotubes took place during the high rate cycling. Even after being cycled at the 5 C rate, using a current density of 2.5 mA cm^{-2} , an areal capacity of $0.24 \text{ mA h cm}^{-2}$, *i.e.* 96 mA h g^{-1} and 52% of that found for the C/10 rate, was still obtained. Moreover, after being cycled at the 5 C rate for more than 500 cycles, an areal capacity of $0.22 \text{ mA h cm}^{-2}$ (*i.e.* 88 mA h g^{-1}), corresponding to 94.5% of the initial value was still obtained. It is also seen that a C/10 rate capacity of $0.460 \text{ mA h cm}^{-2}$ was obtained after the rate capability tests and that the capacity then remained at $0.455 \text{ mA h cm}^{-2}$ after more than 450 cycles, *i.e.* 94% of the initial reversible capacity from the second cycle. These results clearly demonstrate the excellent rate capability and cycling stability of our highly ordered, anatase nanotube electrode, which is very promising for applications in high power density 3D Li-ion microbatteries.

In the 5 C rate cycling experiment discussed above, an extended potential window between 1.2 and 2.5 V *vs.* Li⁺/Li (instead of the normal 1.5 to 2.5 V window) was used to compensate for the increased *iR* drop (see Fig. 3d). As the areal capacity for the normal 1.5 and 2.5 V window was $0.18 \text{ mA h cm}^{-2}$ at the 5 C rate (see Fig. 3c), *i.e.* 75% of the value after the *iR* drop compensation, it is evident that the areal capacities at increased cycling rates depend both on *iR* drop effects and kinetic effects of the lithiation and delithiation reactions. Mass transport limitations within the electrolyte or the nanotubes are clearly unlikely, given the electrolyte concentration and the geometry of the present nanotubular electrode. The characteristic time *t* for Li⁺ ion diffusion is given by $t = L^2/D$ where *L* denotes the diffusion length and *D* the diffusion coefficient.⁴⁰ Given a *D* value for Li⁺ ion diffusion in anatase⁴¹ of $1.81 \times 10^{-13} \text{ cm}^2 \text{ s}^{-1}$ and that *L* for our TiO₂ nanotube electrode is 50 nm (*i.e.* the tube wall thickness), the diffusion time for Li⁺ ions in TiO₂ is only about 1.4 s.

Fig. 4 shows the charge/discharge current density *vs.* areal capacity plots (which correspond to the Ragone power density *vs.* energy density plots) for our highly ordered, anatase TiO₂ nanotube electrodes as well as some previously reported values for other microbattery electrodes. Evidently, our TiO₂ nanotube electrodes show significantly higher power and energy densities, compared to all these previously reported TiO₂-based microbattery electrodes, *i.e.* both the pristine and composite 3D TiO₂ electrodes^{9,10,26–34} and also the 2D TiO₂ electrode.⁴² Owing to the optimized nanotubular array systems, our 9 μm long, highly ordered anatase nanotube electrodes with 50 nm tube wall exhibit a similar rate capability as the short or thin-wall nanotube electrodes,^{27–29} and, more importantly, a significantly higher areal capacity at all the cycling rates.

In Fig. 4, the performance of the commercial Li/LiPON/LiCoO₂ 2D thin-film microbattery⁴³ is also shown to yield lower power and energy densities than our TiO₂ nanotube electrode. In fact, in view of the obtained areal capacity at high and low cycling rates and the cycling stability, the present TiO₂ electrodes show superior microbattery performance compared to most previous 3D microbattery electrodes, including the SnO₂/α-Fe₂O₃ nanotube electrodes,⁴⁴ the PPYDBS/carbon microarray electrodes,¹³ and the LiFePO₄/RVC electrodes.⁴⁵ A more extensive overview

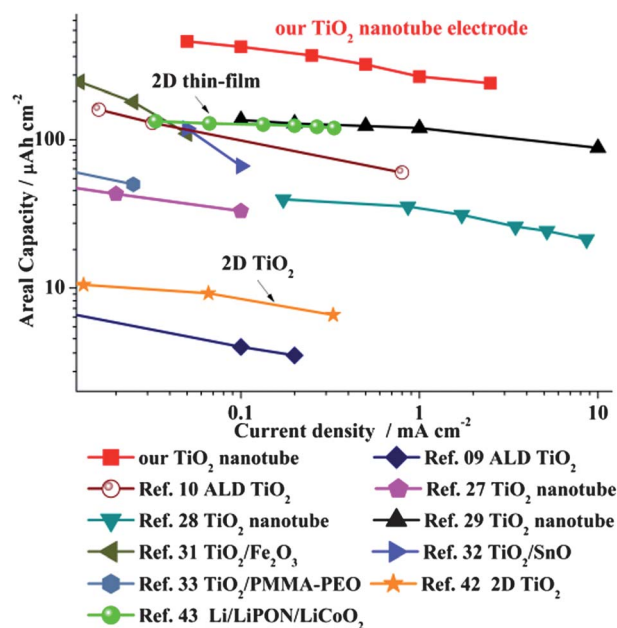


Fig. 4 Areal capacity *vs.* the current density for the present TiO₂ nanotube electrode, other 3D and 2D TiO₂-based microbattery electrodes and the 2D Li/LiPON/LiCoO₂ microbattery.

and comparison of the reported microbattery electrode performances is given in the ESI, Table S4.†

To study the rate performance of our TiO₂ nanotube electrode in more detail, cyclic voltammetry (CV) experiments were carried out on the annealed, two-step anodized TiO₂ nanotube based cell using a potential window between 1.0 and 2.7 V *vs.* Li⁺/Li (or 1.5–2.5 V at low rates) and different scan rates. These results are depicted in Fig. 5a. At a sufficiently slow scan rate (*e.g.*, 0.005 mV s^{-1}), the voltammogram exhibits a pair of well-defined anodic and cathodic peaks, corresponding to the delithiation and lithiation of TiO₂, with a peak potential difference of 148 mV (see the inset of Fig. 5a). The shapes of these peaks are in good agreement with those expected for a reversible surface confined redox reaction.⁴⁶ When the scan rate was increased, the peaks became broader and the difference between the peak potentials increased due to a combination of kinetic and *iR* drop effects.^{11,46}

The potential difference between the anodic and cathodic peaks (ΔE) can therefore be expressed as:

$$\Delta E = A + B \log(I_p) + I_p R \quad (2)$$

where *I_p* denotes the peak current, *A* and *B* are constants, whereas *R* denotes the cell resistance. In Fig. 5b and c, ΔE has been plotted as a function of *I_p* and $\log(I_p)$, respectively, in an attempt to evaluate the influence of the *iR* and kinetic effects. It is seen that linear relationships were found in both Fig. 5b and c for sufficiently low and high currents, respectively. This indicates that ΔE was mainly controlled by *iR* drop effects for scan rates below 0.1 mV s^{-1} while electron transfer kinetic effects dominated at the highest scan rates above 0.1 mV s^{-1} . Since scan rates of 0.1 mV s^{-1} and 1 mV s^{-1} roughly correspond to the

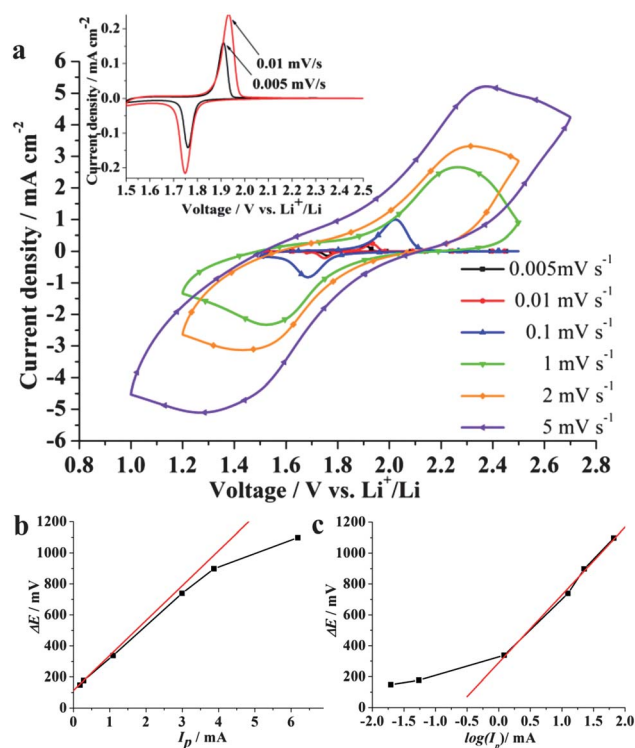


Fig. 5 (a) Cyclic voltammograms recorded for the annealed, two-step anodized TiO_2 nanotube electrode based cell using scan rates between 0.005 and 5 mV s^{-1} . The inset shows a magnification of 0.005 and 0.01 mV s^{-1} . (b) and (c) Plots of I_p vs. ΔE and $\log(I_p)$ vs. ΔE , respectively, using the peak currents and peak potentials evaluated for the different scan rates used in (a).

same time domains as galvanostatic cycling at C/2.8 and 2.8 C rates, it is reasonable to assume that the decreased capacities at high cycling rates depicted in Fig. 3c were mainly caused by electron transfer kinetic effects. This hypothesis is also supported by the fact that only a 15% increase in the capacity was seen when using the iR drop compensated in the 5 C rate cycling experiment. Since the Li^+ insertion and extraction involves structural changes, we attribute these kinetic effects to the overpotentials, *i.e.* the activation energies associated with the structural changes during the lithiation and delithiation of anatase. Since the kinetic effects were mainly seen at scan rates higher than 0.1 mV s^{-1} , it can also be concluded that these structural rearrangements will be practically complete on a time scale longer than ~ 2.3 hours (given the peak potentials of 1.5 and 2.35 V vs. Li^+/Li at a scan rate of 0.1 mV s^{-1}). For higher scan rates, only a fraction of the TiO_2 is consequently electrochemical active, which explains the gradual decrease in the capacity with increasing cycling rate in Fig. 3c.

To investigate the influence of the nanotube dimensions on the capacity and rate capability, battery performance tests were also carried out on the nanotube electrodes with thinner walls and different lengths, respectively. In this work, two approaches were employed to reduce the nanotube wall thickness: post-chemical etching on the formed nanotubes, and growing the nanotubes under modified conditions (*e.g.*, increased fluoride concentration and decreased voltage), respectively. As shown in Fig. 6a and b, $9 \mu\text{m}$ long nanotubes with a wall thickness of 30 nm and an outer diameter of 150 nm could be obtained by etching the two-step anodized nanotube in a 0.2 M NH_4F aqueous solution at 30°C for 4 hours. In addition, approx. $8 \mu\text{m}$

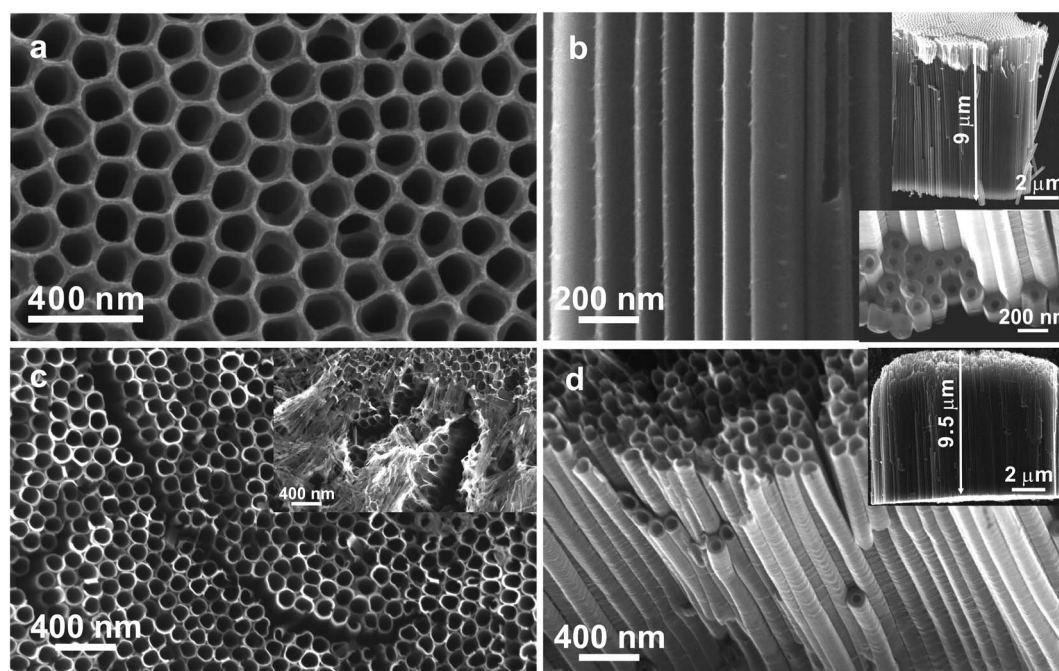


Fig. 6 SEM micrographs for thin wall TiO_2 nanotubes manufactured by (a) and (b) post-chemical etching and (c) and (d) anodization using modified conditions (followed by sonication), showing (a) and (c) top-views and (b) and (d) cross-sectional views. The insets in (b) and (d) show the tube bottoms and lengths. The inset in (c) shows a top-view of the nanotube layer before sonication.

long TiO_2 nanotubes with a wall thickness of 30 nm and an outer diameter of 150 nm were manufactured by two-step anodization of Ti in an ethylene glycol electrolyte containing 0.3 M NH_4F and 5 vol% H_2O at 50 V for 2.5 hours, see Fig. 6c and d. All these nanotube electrodes were annealed prior to the battery experiments.

Fig. 7 compares the electrochemical performances of cells containing annealed, two-step anodized TiO_2 nanotube electrodes with 50 and 30 nm wall thicknesses. As shown in Fig. 7a, the areal capacities for the two TiO_2 nanotube electrodes with 30 nm wall thicknesses were smaller than that found for the corresponding nanotube electrode with 50 nm wall thickness at a rate of $C/10$. A stable areal capacity of $0.36 \text{ mA h cm}^{-2}$ during 100 cycles was obtained with the chemically etched nanotubes. This capacity is in good agreement with the fact that the etched tube electrode contained approximately 70% of the active material present in the nanotube electrode with a wall thickness of 50 nm, that is, the gravimetric capacity of the etched nanotube electrode remained at 184 mA h g^{-1} . The capacity for the other type of 30 nm wall thickness nanotube electrode was, on the other hand, significantly lower than expected and also decreased during the cycling. The initial lower capacity could be explained by the varying length of the nanotubes (caused by the sonication treatment used after the anodization process, see

the Experimental section) which yields a lower amount of TiO_2 . The decreasing capacities during cycling could, on the other hand, be explained by poor adhesion of the nanotubes to the substrate, which was heavily deteriorated by the sonication treatment. The latter was employed to remove the “grassy” nanotube top appearance (see Fig. 6c), which typically is associated with anodization of Ti in electrolytes containing high fluoride concentrations.⁴⁷

The rate performances of these nanotube electrodes are shown in Fig. 7b. It is seen that the ratio between the areal capacities of the nanotube electrodes with 30 nm (obtained by etching) and 50 nm wall thicknesses, respectively, was constant, *i.e.* ~ 0.75 , at various cycling rates. This indicates that there was no significant influence of the tube wall thickness on the rate capability of nanotube electrodes, and further supports the fact that, even by using the thick wall (*e.g.*, 50 nm) nanotube, the excellent rate capability of the nanotube electrodes can still be maintained. For the other nanotube electrodes with 30 nm wall thickness (obtained by modified growth), the areal capacity was found to decrease to almost zero at the 5 C rate and return back to about $0.14 \text{ mA h cm}^{-2}$ when resuming at the $C/10$ rate (the rate capability tests were carried out using the same cells after the 100 cycles tests in Fig. 7a). It is clear that the rate performance of the modified grown nanotubes is significantly lower for the other two nanotubes with either 30 nm or 50 nm wall thickness. This indicates that the rate capability of the nanotube electrodes mainly depends on the ordering of the nanotubes, as this can alter the activation energies of the electron transfer reaction.

Fig. 8 shows the battery performances of the TiO_2 nanotube electrodes with different lengths, *i.e.* 14.5, 9 and 4.5 μm , achieved by adjusting the anodization time. As shown in Fig. 8a, the areal capacity for the 9 μm long nanotube electrode was found to be twice that of the 4.5 μm long nanotube electrode at the $C/10$ rate. Since this is in good agreement with the expectations based on the TiO_2 amount, this result indicates that the entire lengths of the nanotubes were active even for the 9 μm long nanotubes. In other words, the gravimetric capacity of 184 mA h g^{-1} could be maintained for the TiO_2 nanotube electrode with the increased tube length up to 9 μm . The capacity of the 14.5 μm nanotube electrode was likewise initially about 1.5 times larger than that for the 9 μm nanotube electrode, *i.e.* only slightly lower than the ratio of 1.6 based on the ratio of the tube length. Although the latter result may suggest that the full capacity for the 14.5 μm long nanotubes could not be entirely accessed, possibly due to the increased resistance of the long nanotubes, it is immediately evident that the areal capacity at the low cycling rate can be increased by increasing the tube length. For the 14.5 μm long nanotube electrode, an areal capacity of $0.70 \text{ mA h cm}^{-2}$ was hence obtained in the initial cycles which decreased to $0.60 \text{ mA h cm}^{-2}$ after 100 cycles. This capacity fading can be attributed to the relatively weak attachment of the long tubes to the Ti substrate. More importantly, the long term capacity for the 14.5 μm long nanotube electrode was about 30% and 260% higher than that for the 9 and 4.5 μm long nanotube electrodes, respectively.

As is seen in the rate performance data in Fig. 8b, the ratios of the areal capacities between the 9 μm and 4.5 μm long

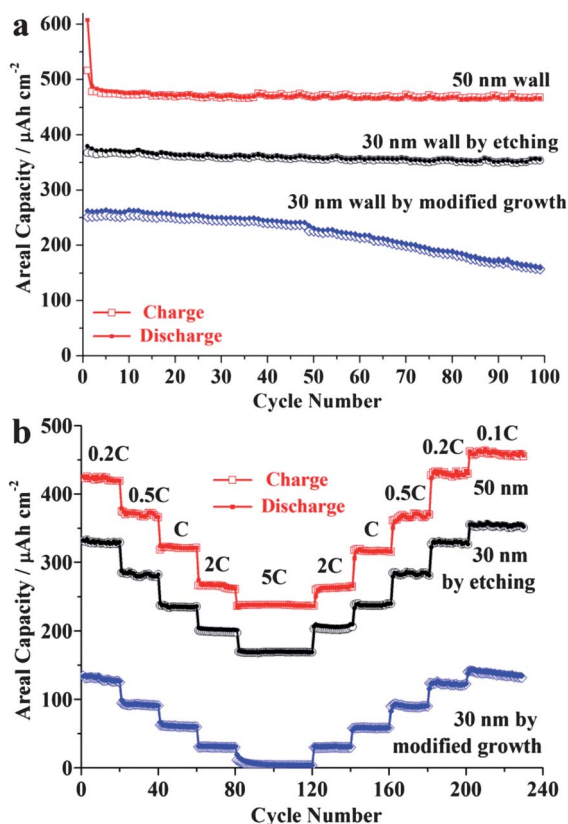


Fig. 7 (a) Galvanostatic areal charge (open symbol) and discharge (solid symbol) capacities as a function of the cycle number for the annealed, two-step anodized nanotube electrodes with tube wall thicknesses of 50 nm, 30 nm by etching, and 30 nm by modified growth, obtained at a $C/10$ rate. (b) Rate capabilities as a function of the cycling rate and cycle number for these nanotube electrodes.

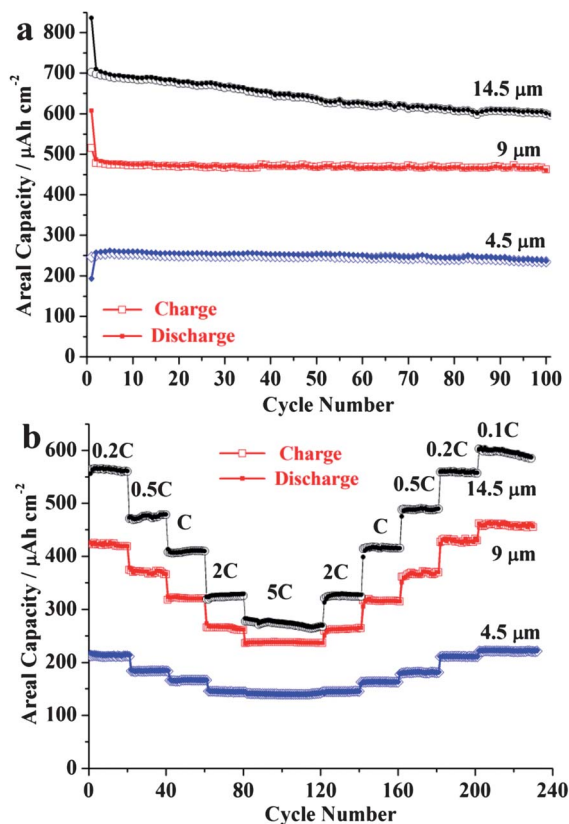


Fig. 8 (a) Galvanostatic areal charge (open symbol) and discharge (solid symbol) capacities as a function of the cycle number for the annealed, two-step anodized nanotube electrodes with tube lengths of 14.5, 9 and 4.5 μm , recorded at a C/10 rate. (b) Rate capabilities as a function of the cycling rate and cycle number for these nanotube electrodes.

nanotube electrodes remained relatively constant at 2 for the various cycling rates. Only at the 5 C rate, this ratio decreased to 1.7. For the 14.5 μm long nanotube electrode, the ratios of the areal capacities between the 14.5 μm and 9 μm long nanotube electrodes were ~ 1.3 at the lower rates and 1.15 at the 5 C rate. As the decreased capacities at the higher rates were found to be more likely to be due to limitations in the electron transfer kinetics (see Fig. 5), these results are in good agreement with the hypothesis that the iR drop only has a minor effect on the rate capability of the nanotube electrodes. This suggests that the areal capacity of the nanotube electrode can be increased by increasing the nanotube length and that the power density (or the rate capability) mainly depends on electron transfer kinetics of the electrode material TiO_2 .

4 Conclusions

Highly ordered, anatase nanotube arrays with a length of 9 μm , obtained by two-step anodization followed by annealing, can provide high and stable areal capacities of $0.24 \text{ mA h cm}^{-2}$ at a charge/discharge current density of 2.5 mA cm^{-2} and $0.46 \text{ mA h cm}^{-2}$ at 0.05 mA cm^{-2} over more than 500 cycles in Li-ion microbatteries. These electrodes thus exhibit significantly better microbattery performance (*i.e.* areal capacities, rate capability,

and cycling stability) than both previously described TiO_2 based electrodes and other 3D microbattery electrodes. It is also clear that the areal capacity can be increased by increasing the tube wall thickness and/or the nanotube lengths, up to 0.6 mA h cm^{-2} for 100 cycles. The cycling stability and the rate capability of the electrodes depend strongly on the long range ordering and crystallinity of the nanotube structures, as the best results were obtained with annealed, two-step anodized nanotube electrodes. Owing to the optimized nanotube systems, the excellent rate capability of electrodes can be maintained even for long tubes with thick tube walls. The rate capability of the present anatase nanotube electrodes is limited mainly by electron transfer kinetics, most likely due to the activation energies associated with the TiO_2 lithiation and delithiation reactions. Given the excellent performance of the present TiO_2 nanotube electrodes, it is clear that these electrodes constitute an excellent platform for the development of full 3D Li-ion microbattery systems.

Acknowledgements

We gratefully acknowledge financial support from the Swedish Research Council (VR), the Swedish Foundation for Strategic Research (SSF), Ångpanneföreningen's Foundation for Research and Development and StandUp for Energy. The Knut and Alice Wallenberg Foundations are acknowledged for an equipment grant for the electron microscopy facilities at Stockholm University. We would also like to thank Henrik Eriksson for valuable technical help and Dr Matthew Roberts for valuable discussions.

References

- 1 J. Bates, N. J. Dudney, B. Neudecker, A. Ueda and C. D. Evans, *Solid State Ionics*, 2000, **135**, 33.
- 2 J. Souquet and M. Duclot, *Solid State Ionics*, 2002, **148**, 375.
- 3 J. W. Long, B. Dunn, D. R. Rolison and H. S. White, *Chem. Rev.*, 2004, **104**, 4463.
- 4 D. R. Rolison, J. W. Long, J. C. Lytle, A. E. Fischer, C. P. Rhodes, T. M. McEvoy, M. E. Bourg and A. M. Lubers, *Chem. Soc. Rev.*, 2009, **38**, 226.
- 5 M. Roberts, P. Johns, J. Owen, D. Brandell, K. Edström, G. Enany, C. Guery, D. Golodnitsky, M. Lacey, C. Lecoeur, H. Mazar, E. Peled, E. Perre, M. M. Shaijumon, P. Simon and P. L. Taberna, *J. Mater. Chem.*, 2011, **21**, 9876.
- 6 T. S. Arthur, D. J. Bates, N. Cirigliano, D. C. Johnson, P. Malati, J. M. Mosby, E. Perre, M. T. Rawls, A. L. Prieto and B. Dunn, *MRS Bull.*, 2011, **36**, 523.
- 7 J. F. M. Oudenhoven, L. Baggetto and P. H. L. Notten, *Adv. Energy Mater.*, 2011, **1**, 10.
- 8 M. M. Shaijumon, E. Perre, B. Daffos, P. L. Taberna, J. M. Tarascon and P. Simon, *Adv. Mater.*, 2010, **22**, 4978.
- 9 S. K. Cheah, E. Perre, M. Rooth, M. Fondell, A. Hårsta, L. Nyholm, M. Boman, J. Lu, P. Simon and K. Edström, *Nano Lett.*, 2009, **9**, 3230.
- 10 W. Wang, M. Tian, A. Abdulagatov, S. M. George, Y. C. Lee and R. Yang, *Nano Lett.*, 2012, **12**, 655.

- 11 P. L. Taberna, S. Mitra, P. Poizot, P. Simon and J. M. Tarascon, *Nat. Mater.*, 2006, **5**, 567.
- 12 H. Mazor, D. Golodnitsky, L. Burstein, A. Gladkikh and E. Peled, *J. Power Sources*, 2012, **198**, 264.
- 13 H. S. Min, B. Y. Park, L. Taherabadi, C. Wang, Y. Yeh, R. Zaouk, M. J. Madou and B. Dunn, *J. Power Sources*, 2008, **178**, 795.
- 14 P. Roy, S. Berger and P. Schmuki, *Angew. Chem., Int. Ed.*, 2011, **50**, 2904.
- 15 W. Wei, K. Lee, S. Shaw and P. Schmuki, *Chem. Commun.*, 2012, **48**, 4244.
- 16 R. R. Rangaraju, K. S. Raja, A. Panday and M. Misra, *Electrochim. Acta*, 2010, **55**, 785.
- 17 L. Shen, E. Uchaker, X. Zhang and G. Cao, *Adv. Mater.*, 2012, **24**, 6502.
- 18 B. Zachau-Christiansen, K. West, T. Jacobsen and S. Atlung, *Solid State Ionics*, 1988, **28–30**, 1176.
- 19 S. Y. Huang, L. Kavan, I. Exnar and M. Grätzel, *J. Electrochem. Soc.*, 1995, **142**, L142.
- 20 J. Li, Z. Tang and Z. Zhang, *Electrochem. Commun.*, 2005, **7**, 62.
- 21 A. R. Armstrong, G. Armstrong, J. Canales, R. Garcia and P. G. Bruce, *Adv. Mater.*, 2005, **17**, 862.
- 22 L. Kavan, M. Kalbac, M. Zúkalová, I. Exnar, V. Lorenzen, R. Nesper and M. Grätzel, *Chem. Mater.*, 2004, **16**, 840.
- 23 K. Wang, M. Wei, M. A. Morris, H. Zhou and J. D. Holmes, *Adv. Mater.*, 2007, **19**, 3016.
- 24 J. Y. Shin, D. Samuelis and J. Maier, *Adv. Funct. Mater.*, 2011, **21**, 3464.
- 25 H. Han, T. Song, E. K. Lee, A. Devadoss, Y. Jeon, J. Ha, Y. C. Chung, Y. M. Choi, Y. G. Jung and U. Paik, *ACS Nano*, 2012, **6**, 8308.
- 26 D. Liu, P. Xiao, Y. Zhang, B. Garcia, Q. Zhang, Q. Guo, R. Champion and G. Cao, *J. Phys. Chem. C*, 2008, **112**, 11175.
- 27 G. F. Ortiz, I. Hanzu, T. Djenizian, P. Lavela, J. L. Tirado and P. Knauth, *Chem. Mater.*, 2009, **21**, 63.
- 28 H. T. Fang, M. Liu, D. W. Wang, T. Sun, D. S. Guan, F. Li, J. Zhou, T. K. Sham and H. M. Cheng, *Nanotechnology*, 2009, **20**, 225701.
- 29 W. H. Ryu, D. H. Nam, Y. S. Ko, R. H. Kim and H. S. Kwon, *Electrochim. Acta*, 2012, **61**, 19.
- 30 J. González, R. Alcántara, F. Nacimiento, G. F. Ortiz, J. L. Tirado, E. Zhecheva and R. Stoyanova, *J. Phys. Chem. C*, 2012, **116**, 20182.
- 31 G. F. Ortiz, I. Hanzu, P. Lavela, J. L. Tirado, P. Knauth and T. Djenizian, *J. Mater. Chem.*, 2010, **20**, 4041.
- 32 T. Djenizian, I. Hanzu and P. Knauth, *J. Mater. Chem.*, 2011, **21**, 9925.
- 33 N. A. Kyeremateng, F. Dumur, P. Knauth, B. Pecquenard and T. Djenizian, *Electrochem. Commun.*, 2011, **13**, 894.
- 34 L. Yu, Z. Wang, L. Zhang, H. B. Wu and X. W. Lou, *J. Mater. Chem. A*, 2013, **1**, 122.
- 35 G. G. Zhang, H. T. Huang, Y. H. Zhang, H. L. W. Chan and L. M. Zhou, *Electrochem. Commun.*, 2007, **9**, 2854.
- 36 D. V. Bavykin, M. Carravetta, A. N. Kulak and F. C. Walsh, *Chem. Mater.*, 2010, **22**, 2458.
- 37 S. P. Albu, H. Tsuchiya, S. Fujimoto and P. Schmuki, *Eur. J. Inorg. Chem.*, 2010, **2010**, 4351.
- 38 M. Wagemaker, R. van de Krol, A. P. Kentgens, A. van Well and F. M. Mulder, *J. Am. Chem. Soc.*, 2001, **123**, 11454.
- 39 K. Xu, *Chem. Rev.*, 2004, **104**, 4303.
- 40 P. G. Bruce, B. Scrosati and J. M. Tarascon, *Angew. Chem., Int. Ed.*, 2008, **47**, 2930.
- 41 L. Kavan, K. Kratochvilová and M. Grätzel, *J. Electroanal. Chem.*, 1995, **394**, 93.
- 42 M. J. Lindsay, M. G. Blackford, D. J. Attard, V. Luca, M. Skyllas-Kazacos and C. S. Griffith, *Electrochim. Acta*, 2007, **52**, 6401.
- 43 G. Nagasubramanian and D. H. Doughty, *J. Power Sources*, 2004, **136**, 395.
- 44 W. Zeng, F. Zheng, R. Li, Y. Zhan, Y. Li and J. Liu, *Nanoscale*, 2012, **4**, 2760.
- 45 M. Roberts, A. F. Huang, P. Johns and J. Owen, *J. Power Sources*, 2013, **224**, 250.
- 46 A. J. Bard and L. R. Faulkner, *Electrochemical Methods*, Wiley, New York, 2nd edn, 2001.
- 47 L. Sun, S. Zhang, X. Wang, X. W. Sun, D. Y. Ong, X. Wang and D. Zhao, *ChemPhysChem*, 2011, **12**, 3634.